



ORIGINAL ARTICLE

Preparation of N-acetyl-para-aminophenol via a flow route of a clean amination and acylation of p-nitrophenol catalyzing by core-shell $\text{Cu}_2\text{O}@ \text{CeO}_2$



Yue Li ^{a,b,1}, Yuxuan Ma ^{a,1}, Yuanyuan Zhang ^a, Xiaojing Wang ^{a,*}, Fenghua Bai ^{a,c,*}

^a Inner Mongolia Key Laboratory of Chemistry and Physics of Rare Earth Materials, School of Chemistry and Chemical Engineering, Inner Mongolia University, Hohhot, Inner Mongolia, China

^b Key Laboratory of Microsystems and Microstructures Manufacturing, Ministry of Education, Micro/Nanotechnology Research Centre, Harbin Institute of Technology, Yi Kuang Jie 2, Harbin 150080, China

^c Key Laboratory of Advanced Energy Materials Chemistry (Ministry of Education), College of Chemistry, Nankai University, Tianjin 300071, China

Received 30 July 2020; accepted 21 September 2020

Available online 7 October 2020

KEYWORDS

Core-shell $\text{Cu}_2\text{O}@ \text{CeO}_2$;
Paracetamol;
P-nitrophenol;
P-anomiphenol;
Selective conversion

Abstract The selectivity and reactivity to converse series nitroaromatic into aminobenzenes are especially significant, which play a vital role in synthesizing required drugs or other fine chemicals. Herein, p-nitrophenol (p-NP) has been completely converted into p-anomiphenol (p-AP) with a high activity factor k ($0.033 \text{ s}^{-1} \cdot \text{mg}^{-1}$) and reusability by core-shell $\text{Cu}_2\text{O}@ \text{CeO}_2$ catalyst. N-acetyl-para-aminophenol (paracetamol, APAP) as a model drug was further synthesized via a flow route proceeded in two steps including p-NP reduction and subsequently p-AP acylation with self-constructing device. The yield of the paracetamol is up to 85% with a highly purity. The mechanism investigation justifies the rich-electron centers and cation defects generated from the redox coupled $\text{Cu}^+ \rightarrow \text{Cu}^0$ with $\text{Ce}^{3+} \rightarrow \text{Ce}^{4+}$ will steer selective conversion of p-NP to p-AP, a rate-determining step in the production of APAP. The present results could visualize a highly selective catalyst and a new synthesis route for pharmaceuticals such as paracetamol by using nitroaromatic com-

* Corresponding authors at: Inner Mongolia Key Laboratory of Chemistry and Physics of Rare Earth Materials, School of Chemistry and Chemical Engineering, Inner Mongolia University, Hohhot, Inner Mongolia, China.

E-mail addresses: wang_xiao_jing@hotmail.com (X. Wang), f.h.bai@imu.edu.cn (F. Bai).

¹ Y.L. and Y.X.M. are cofirst authors.

Peer review under responsibility of King Saud University.



pounds as the raw materials with environment-friendly, low-cost, easy-manipulation, high-efficiency and high purity.

© 2020 The Authors. Published by Elsevier B.V. on behalf of King Saud University. This is an open access article under the CC BY-NC-ND license (<http://creativecommons.org/licenses/by-nc-nd/4.0/>).

1. Introduction

The key reactive step of fine chemicals synthesis such as drugs, pesticides, herbicides, and dyes with nitroaromatics as the initial raw materials by the heterogeneous catalytic route is selective conversion of nitroaromatics to corresponding aniline derivatives (Corma and Serna, 2006; Song et al., 2018). It is consensus that loading active noble metal with strong affinity for hydrogen on the support is more effective to converse nitrobenzenes into the aminobenzenes directly and they are widely used in various pharmaceutical and fine chemical factories. The typical reported catalysts, such as Pt/CNT (Li et al., 2018), Pt NPs/carbon nanofibers (CNFs) (Takasaki et al., 2008), Pt/TiO₂ (Macino et al., 2019) NPs/zinc oxide nanorods (Han et al., 2019), Pd NPs/Fe₂O₃ (Shokouhimehr et al., 2018), Pd NPs/activated carbon (Sun et al., 2014), Au/PAN (Liu et al., 2015), Au NPs/silica (Wang et al., 2014), Fe₃O₄@-polyaniline@Au (Xuan et al., 2009) Au NPs/TiO₂ or Fe₂O₃ (Fountoulaki et al., 2014; Ren et al., 2017); graphene oxide/Ag/CeO₂ (Ji et al., 2014), Ag NPs/BCN (Qiu et al., 2016), Ag NPs/Reduced graphene oxide (Reddy et al., 2018; Shimizu et al., 2010), and Fe₃O₄@PPy-MAA/Ag (Das et al., 2019); all present the accelerated reactive proceeding. Nevertheless, the conversion of nitrobenzene to the corresponding aniline usually produces more possible byproducts, which originated from the intermediates of the reduction of -NO₂ functional groups and the following coupling, such as hydroxylamine intermediates, azo and azo, etc (Serna and Corma, 2015). In such situation, the purity for the further synthesis of the required drug or other fine chemicals is bound to be significantly limited. Therefore, to develop the catalysts for highly efficient and regioselective conversion of nitro to amino groups under mild reaction conditions is actively pursued for the industrialization application.

Furthermore, taking into consideration of expensive and rare scarcity of noble metal, the earth rich, stable and well performance non-noble-metal catalysts, such as CuFe₂O₄ (Zhuang et al., 2017); BiOCl (Formenti et al., 2019), Co₃O₄ (Chen et al., 2017); NiCo (Bai et al., 2012); ZnO (Wang and Astruc, 2017), have been well developed. Recently, copper oxides (copper, CuO and Cu₂O) taking advantages of nontoxic, highly abundant and low-cost, have drawn the attention of researchers due to its prominent optical, electronic, and catalytic properties. It is suggested in several reported references that copper-based materials are very possible as cheap alternates for noble metals in numerous applications (Christians et al., 2014; Zhang et al., 2019; Ozel et al., 2016). For instance, Cu₂O with suitable band gap energy (2.0–2.2 eV) and more energetic conduction band (~1.0 eV) has shown a very effective function on the process of catalytic reduction of nitrobenzene (Toe et al., 2018; Lum and Ager, 2018). In addition, in such industrial application, the long-term stability of the catalysts should also be specially considered. It has been reported that the embedding small-sized noble metal nanoparticles into

highly stable metal oxides is an effective strategy to improve stability because the shell of the metal oxides could keep their original shape and hinder their direct contact with the air (Wu et al., 2016). In addition, the further investigation indicated that the electrochemical and catalytic activity can be improved by assembling a cerium oxide shell (for example, CeO₂-encapsulated Au nanostructures, tunable bimetallic Au-Pd@CeO₂, core-shell Au@CeO₂ nanocomposites, Pt/CeO₂ hybrid nanostructures, highly catalytic active Au-CeO₂@ZrO₂ yolk-shell nanocomposites, modify of Pt on Cu/Co bimetallic doping CeO₂ nanospheres) (Li et al., 2018; Song et al., 2017; Evangelista et al., 2015; Wang et al., 2016; Liu et al., 2019; Qi et al., 2012). Inspiring by these researches, a Cu-based material with CeO₂ as an effective protective shell should be very prospective to catalyze nitrobenzenes to the corresponding amino series.

Paracetamol (APAP) is an important drug which is used for the relief of pain and fever. A relative inert p-NP as a starting reactant via an intermediate p-AP is frequently used to synthesize APAP whereas it is also followed with the formation of organic impurities inevitably, such as hydroxylamine, hydrazine, or azoarene (Magadum and Yadav, 2018; Arulraj et al., 2015). Undoubtedly, as the rate-determining step in the production process of APAP the completely selective reduction of p-NP to p-AP has great significance on a higher purity. Recently, several research groups reported that alkylated anilines can be synthesized from nitroarenes by using alcohols as the alkyl-source in the presence of (P ~ N)Ru(CO)₂Cl₂ (Xu et al., 2009); [Ru(p-cymene)Cl₂]₂ (Haniti et al., 2009) and Ag/Al₂O₃ (Blaser et al., 2009). However, due to the steric hindrance of the alkylating agent, primary amines are more likely to be formed during the alkylation process, so the selectivity is poor. It has also been noted that to prepare APAP by in-situ hydrogenation of nitrobenzene over Raney-Ni catalyst followed by an alkylation, the major drawbacks were low efficiency with a large quantity of catalysts (370–440 mol% Raney Ni with respect to nitrobenzene), harsh reaction conditions and long reaction time (Rong et al., 2013). Moreover, it needs special attention in this design that the production process of APAP is impossible achieved for the reduction of p-NP and acylation of p-AP simultaneously because the conversion of p-NP to p-AP is under alkaline environment and the acylation of p-AP is acidification. In contrast, intermediates' separation and purification are followed arduous tasks. Remarkably, a favorable protocol is very valuable to rapidly synthesize APAP in a flow approach without purification process and be compatible with alkaline reduction and acid acylation to avoid the high cost, serious pollution, and special catalytic conditions required in traditional preparation process.

In this work, a simple flow procedure was designed to synthesize APAP from an inert p-NP. A core-shell Cu₂O@CeO₂ catalyst was prepared to highly effectively and selectively converse p-NP into p-AP. Then the followed alkylation process of p-AP was smoothly performed through a well self-assembly

device without purifying. Furthermore, the reactant, intermediate and product have been well characterized by using IR, LC-MS, and H-NMR techniques. Eventually, a reactive mechanism was proposed.

2. Materials and methods

2.1. Materials

All reagents used in this study are all of analytical grade. For methanol, the chromatographic-grade is used. Hexamethylenetetramine (HMTA) and p-NP were purchased from Shanghai Aladdin Industrial Corporation. Hydroxylamine hydrochloride ($\text{NH}_2\text{OH}\cdot\text{HCl}$), sodium hydrogen sulfite (NaHSO_3), and potassium hydroxide (KOH) were obtained from Macklin. Isopropyl alcohol cupric chloride ($\text{CuCl}_2\cdot 6\text{H}_2\text{O}$) were purchased from Beijing Innochem.

2.2. Method

2.2.1. Fabrication of CeO_2

CeO_2 NPs were prepared by solid phase grinding at room temperature. 0.01 mol $\text{Ce}(\text{NO}_3)_3\cdot 6\text{H}_2\text{O}$ was milled together with 12 g KOH to synthesize $\text{Ce}(\text{OH})_4$ in a agate mortar at the ambient pressure for half an hour. Washed with deionized water and ethanol until $\text{Ce}(\text{OH})_4$ showed neutral. Then, the suspension was dried for 12 h in a petri dish under vacuum at 373 K. Finally, a grayish yellow powder of CeO_2 was obtained.

2.2.2. Fabrication of core-shell $\text{Cu}_2\text{O}@/\text{CeO}_2$

The core-shell $\text{Cu}_2\text{O}@/\text{CeO}_2$ was synthesized by aqueous phase reduction. 0.025 mol·L⁻¹ NaOH was added into seven beakers respectively, which contained 10 mL 0.2 mol·L⁻¹ $\text{CuCl}_2\cdot 2\text{H}_2\text{O}$ solution. 1.4 g $\text{NH}_2\text{OH}\cdot\text{HCl}$ was dissolved in 10 mL water and then was added to above suspensions drop by drop. After stirring for half an hour, fresh cuprous oxide particles are formed. At the same time, the color of the reaction tank turns reddish brown. 0.01 M HMTA was added to

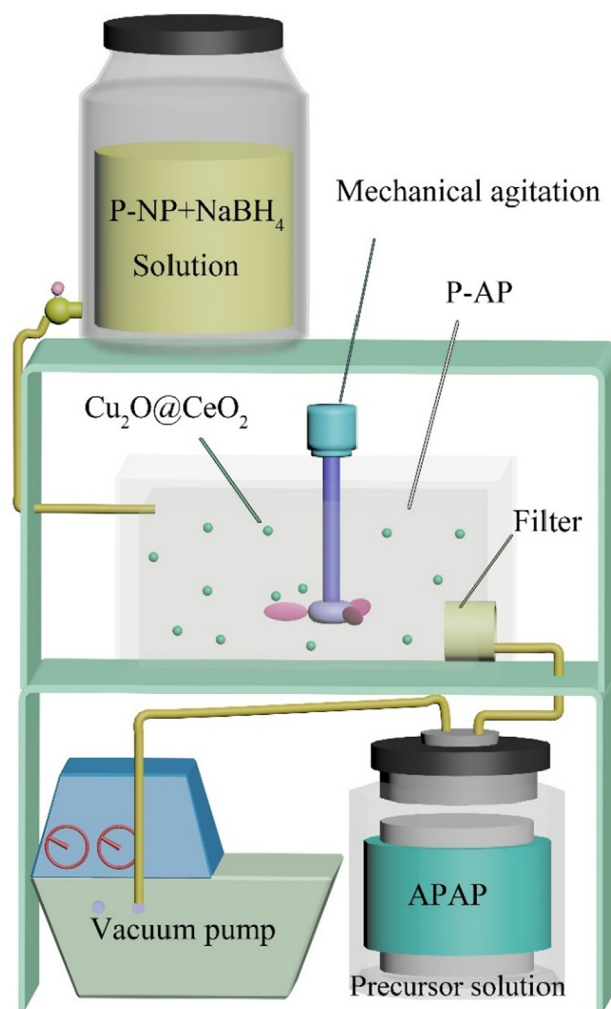


Fig. 1 The experimental device of producing APAP from p-NP.

the above suspension with the different ratios of cuprous oxide. Then, 0.4 mmol, 0.8 mmol, 1.2 mmol, 1.6 mmol,

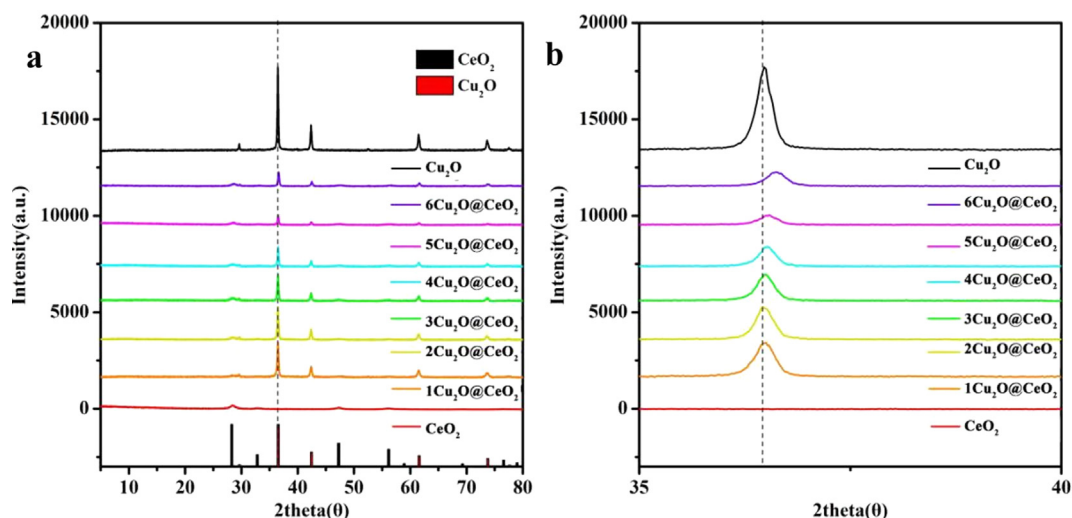


Fig. 2 XRD patterns of CeO_2 , Cu_2O and $\text{Cu}_2\text{O}@/\text{CeO}_2$ composites (a), the amplified image of peak (002) of Cu_2O (b).

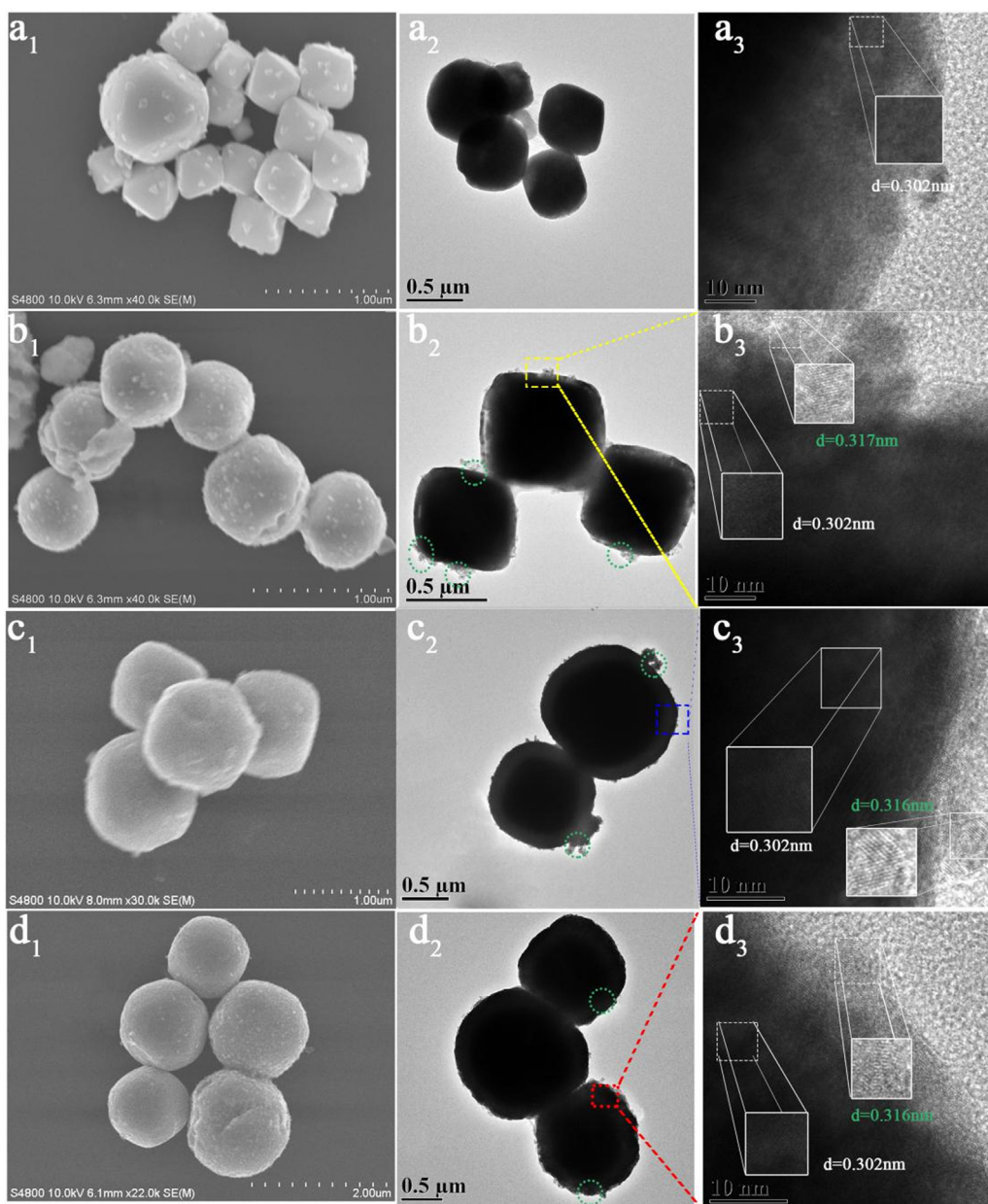


Fig. 3 SEM, TEM and HRTEM images of Cu_2O (a1, a2, a3) and $2\text{Cu}_2\text{O}@/\text{CeO}_2$ (b1, b2, b3), $3\text{Cu}_2\text{O}@/\text{CeO}_2$ (c1, c2, c3) and $4\text{Cu}_2\text{O}@/\text{CeO}_2$ (d1, d2, d3).

2.0 mmol, and 2.4 mmol $\text{Ce}(\text{NO}_3)_3 \cdot 6\text{H}_2\text{O}$ were dissolved in 10 mL water respectively, which were poured into the as-prepared solution. The obtained suspensions were adjusted to alkaline by using NaOH solution. The products were washed with deionized water and ethanol several times until Na^+ and Cl^- ions were not detected. Finally, the products were obtained after drying in vacuum at 373 K. The obtained products were donated as $1\text{Cu}_2\text{O}@/\text{CeO}_2$, $2\text{Cu}_2\text{O}@/\text{CeO}_2$, $3\text{Cu}_2\text{O}@/\text{CeO}_2$, $4\text{Cu}_2\text{O}@/\text{CeO}_2$, $5\text{Cu}_2\text{O}@/\text{CeO}_2$, and $6\text{Cu}_2\text{O}@/\text{CeO}_2$, respectively.

2.3. Evaluation the reduction p-NP efficiency

To evaluate the conversion rate of p-NP to p-AP with the as-prepared nanocomposites, 0.03 mL of p-NP ($0.01 \text{ mol} \cdot \text{L}^{-1}$) and

0.2 mL NaBH_4 ($0.5 \text{ mol} \cdot \text{L}^{-1}$) were mixed in a 5 mL quartz cuvette reactor. To start the reaction, 5 mg of Cu_2O , CeO_2 , $1\text{Cu}_2\text{O}@/\text{CeO}_2$, $2\text{Cu}_2\text{O}@/\text{CeO}_2$, $3\text{Cu}_2\text{O}@/\text{CeO}_2$, $4\text{Cu}_2\text{O}@/\text{CeO}_2$, $5\text{Cu}_2\text{O}@/\text{CeO}_2$ and $6\text{Cu}_2\text{O}@/\text{CeO}_2$ were added to above solution, respectively. After in the presence of the catalyst, the obtained solution was tested by UV-vis spectrometer. The absorption peak at 400 nm is p-NP ion while the one at 300 nm belongs to p-AP (Lum and Ager, 2018). To assess the reusable stability, 0.03 mL p-NP ($0.01 \text{ mol} \cdot \text{L}^{-1}$) solution was added to the reactor for 30 turns.

2.4. Batch experiment and synthesis of APAP

Then, the batch experiment was implemented with a self-designed experimental device as shown in Fig. 1. Firstly,

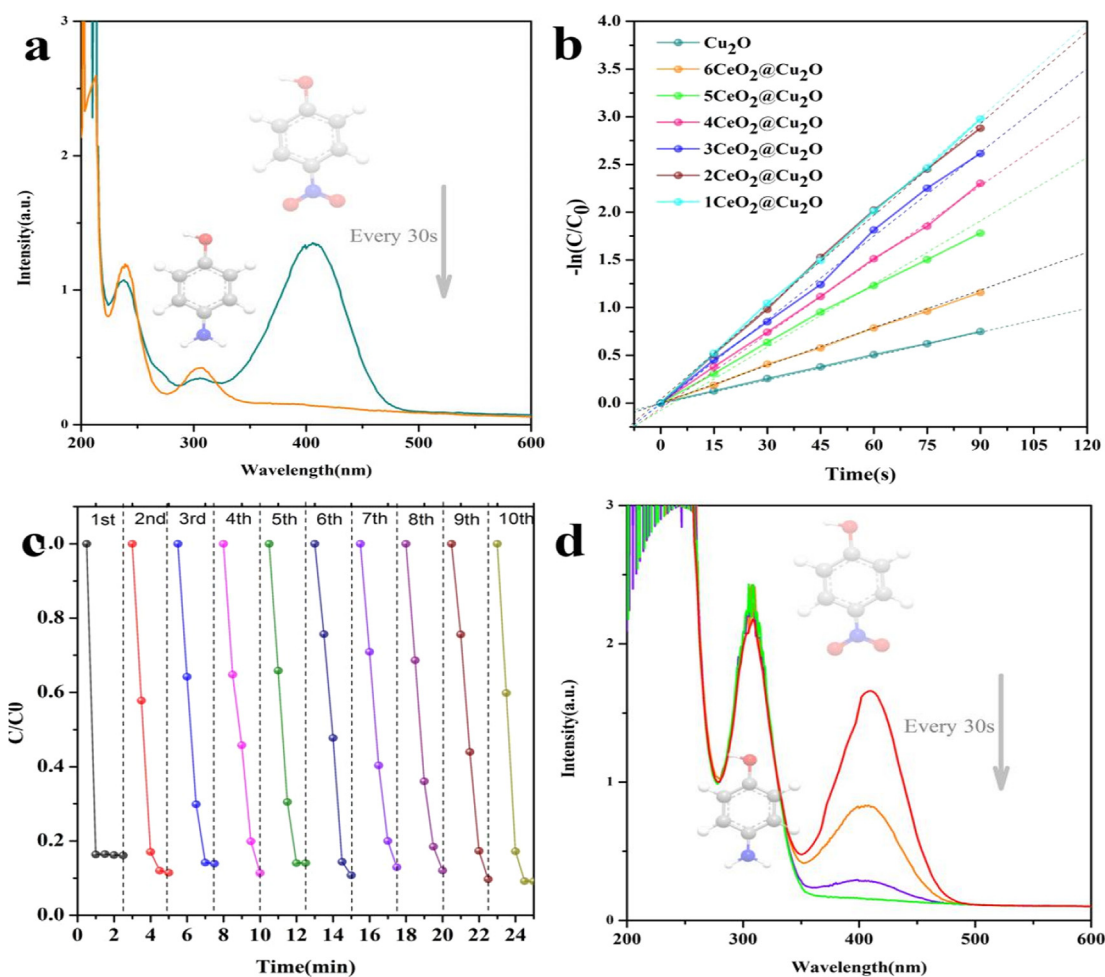


Fig. 4 Reduction of p-NP to p-AP with 3Cu₂O@CeO₂ (a) and the corresponding kinetics plots by using a series of Cu₂O@CeO₂ (b), the durability of 3Cu₂O@CeO₂ for 30 recycle tests (c) and the activity of the used 3Cu₂O@CeO₂ after 30th cycle (d).

20 g of p-NP was completely dissolved in 10 L warm water by mechanical agitation. Then, 1 g catalyst was added to the system together with 4 L NaBH₄ (0.5 mol·L⁻¹) solution. Afterwards, the p-NP was quickly converted into p-AP. The recovered p-AP liquid was collected and acidified in the Teflon containers with 28 mL concentrated hydrochloric acid, 25.6 mL acetic anhydride and 100 mL solution sodium acetate. The solution was stirred vigorously in an ice bath. At the same time, the insoluble APAP particles were formed and washed with a small amount of distilled water after vacuum filtration. The crude product was mixed with 100 mL water and then heated until the suspension boiled and dissolved. After the solution cooled down, 1 g activated carbon was added, and then heated for 5 min. The filtrate was placed in a -10 °C refrigerator for recrystallization and filtration, and the filter precipitate was washed three times with NaHSO₃ and dried. The final APAP quality is 18.49 g.

2.5. Characterization

The crystalline phases of samples were characterized by X-ray diffraction (XRD) with a scan rate of 2° min⁻¹ in 2θ range from 5° to 80°. The morphology of the samples was obtained

using the scanning electron microscopy (SEM HITACHI S-4800) and transmission electron microscopy (TEM Tecnai G2 F20 S-TWIN). UV-vis absorption spectra of the powder samples were measured in the range of 200–800 nm with a diffusive reflectance. During the reaction, UV-visible spectrophotometer (SPECORD 50 N) were used to measure the reactive solution and the spectra value was recorded in the range of 200–800 nm. Measurements were taken with a 0.005 V amplitude in the frequency range of 0.01–105 Hz under ambient light. In situ Infrared spectroscopy (Vertex 70v-Bruker) was used to judge the surface information of the catalysts during the reactive procedure. The nuclear magnetic resonance hydrogen spectrometer (H-NMR 400-Bruker) was used to detect molecular structure where the solvent is DMSO and water. Liquid chromatograph-mass spectrometer (LC-MS 2020-Shimadzu) provided component analysis and nucleoplasmic ratio results. Gradient elution was used during the test. The mobile phase was methanol and water in different proportions, and the injection volume was 10 μL. The column temperature of the liquid chromatography is 40 °C and the detection wavelength of the column is 254 nm. The positive and negative proton peaks were set in the range of 90–350 ^q/_m in order to accurately determine the relative molecular mass of products.

3. Results and discussion

3.1. Catalyst's structure and morphology

Fig. 2a shows XRD patterns of CeO₂, Cu₂O and as-prepared Cu₂O@CeO₂. The diffraction peaks located at 28.5°, 33.0°, 47.4°, and 56.3° are indexed to lattice planes (111), (002), (022), and (113) of CeO₂, respectively, which corresponds to JCPDS No. 98-006-3194. For Cu₂O@CeO₂, no other peaks were detected except for Cu₂O and CeO₂ in the XRD patterns. Meanwhile, CeO₂ peaks are broadened while the Cu₂O peaks located at 36.4° are sharp, being attributed to the highly dispersity of CeO₂ and high crystallinity of Cu₂O. Obviously, with the increasing proportion of CeO₂, the peak (002) of Cu₂O shifts to the right and the crystallinity drops significantly

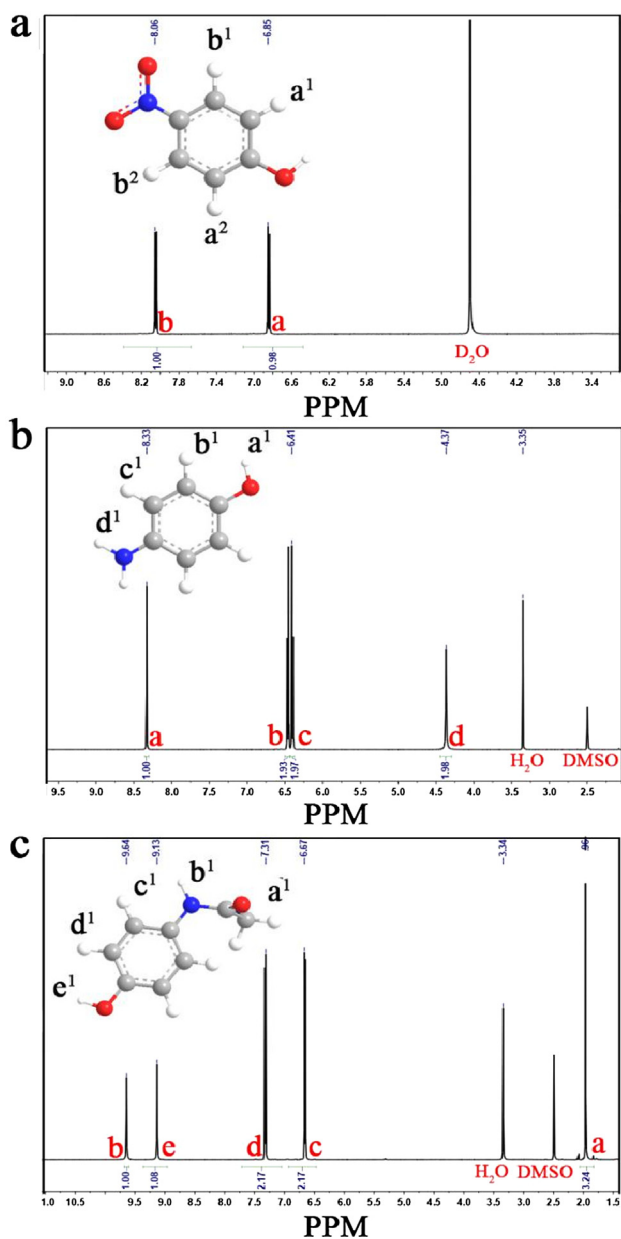


Fig. 5 ¹H NMR spectra of p-NP (a), p-AP (b) and APAP (c).

in Fig. 2b. This result indicates that CeO₂ is not only doped into the cuprous oxide lattice, but also reduces its crystallinity.

Morphology of Cu₂O and Cu₂O@CeO₂ viewed by SEM, TEM, and HRTEM are shown in Fig. 3. It can be observed that Cu₂O presents nonuniform octahedral morphology while pure CeO₂ is the fine rod-like particle with a diameter of ~40–100 nm (Fig. 3a1, a2, a3 and Fig. S1). Typically, for the composite Cu₂O@CeO₂, the octahedral Cu₂O is uniformly packaged by CeO₂ NPs in a closely combination way (Fig. 3b, c, and d). The measured lattice stripes of 0.302 nm and 0.312 nm in HRTEM images correspond to the (110) plane of Cu₂O and (111) plane of CeO₂, respectively. By observing the TEM images of the light and dark contrast, it is remarkably that with the increasing amount of CeO₂, the shell of CeO₂ gradually thickens. Moreover, the gradually wrapped structure by CeO₂ on Cu₂O could be convinced with an EDX mapping analysis which shows a little amount of copper element is exposed to the outside surface of the composite (Fig. S2). Thus, the catalysts were assembled into a corrugated sphere with tiny CeO₂ NPs coated on the surface of the dodecahedron Cu₂O.

3.2. The catalytic activity assessment of the as-prepared Cu₂O@CeO₂ for synthesis of APAP

Firstly, the selective reduction of p-NP to p-AP is particularly significant for its further application because the various intermediates are generally produced during the conversion process of p-NP to p-AP, which may especially influence the productivity and purity of the coming product APAP. Thereby, we estimated the selective reduction of p-NP to p-AP with a series of Cu₂O@CeO₂ in NaBH₄ aqueous medium. Obviously in our system, although Cu₂O (Fig. S3a) and CeO₂ (Fig. S3b) could not make the reaction proceed smoothly, consistent with the previous reports (Ji et al., 2014; Huang et al., 2014; Yu et al., 2010), the conversion of p-NP to p-AP with 3Cu₂O@CeO₂ is achieved within only 0.5 min (Fig. 4a). In Fig. 4b, the $\ln(C_0/C_t) = k_{app}t$ plots present a linear relationship against time, where k_{app} is the apparent rate constant and C_0 and C_t are the initial and actual concentration of p-NP at time t_0 and t , respectively. It clearly indicates that the reaction follows a pseudo-first-order kinetic at excess initial concentration of NaBH₄. Then, the activity factor of Cu₂O@CeO₂ is calculated by the formula $k = k_{app}/m$, ratio of k_{app} to the total mass m of the catalyst which listed in Table S1. One can see the activity factor k range from 0.013 to 0.033 s⁻¹·mg⁻¹ for Cu₂O@CeO₂ composites in this investigation, obviously larger than that of Cu₂O (0.0083 s⁻¹·mg⁻¹). Furthermore, a reusable possibility of Cu₂O@CeO₂ was carefully estimated in the reduction of p-NP with NaBH₄. The eminent durability is easily confirmed by 10 turns of Cu₂O@CeO₂ (Fig. 4c) and even 30 recyclable turns (Fig. S4). More importantly, the sole peak at 300 nm is observed both before and after the 30th reaction (Fig. 4a and d), inferring that the clean conversion without any byproducts always is maintained during the reductive process.

In the subsequently reactive step, APAP was prepared by acylation reaction under low temperature conditions. For the best productivity and purity of APAP, the absolutely selective conversion of p-NP to p-AP and to avoid the further coupled occurrence of p-AP is especially necessary. In our designed

reactive routes, the generated p-AP was directly transported to the connected Teflon vessel without recrystallization and then promptly acidified with a mixed solution of hydrochloric acid, acetic anhydride and solution sodium acetate. Finally, in terms of its weak solubility, the final product of APAP is well separated from the solution with a negative pressure method in ice bath reactor. ^1H NMR spectrum was further used to identify the productivity and purity and the measured results are shown in Figs. 5 and 6. The phenolic proton appears at $d = 10.77$ ppm for initial p-NP and it is disappeared after reduction process due to the formation of hydrogen bond with one nitrogen atom of phenol (Fig. 5a). The chemical shifts in the ^1H NMR spectrum of the reduced intermediate p-AP corre-

spond to $d = 4.31$, $d = 6.41$, and $d = 8.33$ which are similar with that of p-NP (Fig. 5b), except for the doublets located at $d = 6.85$ ppm and $d = 8.08$ ppm, respectively. For the final APAP, the chemical shifts correspond to $d = 1.96$, $d = 6.67$, $d = 7.31$, $d = 9.13$, and $d = 9.64$ (Fig. 5c). Consequently, all the proton quality ratio of intermediates and products correspond to the framework of the p-AP and APAP, indicating that there no impurities in the purified APAP (Tsuji et al., 2017; Zhao et al., 2019). HPLC-MS analysis shows the appearance of APAP with retention times $R_t = 0.65$ min (Fig. 6a). The identity of APAP are distinctly ascertained by the occurrence of characteristic protonated pseudo molecular ions with ($m/z + \text{H} +$) values of 150.10

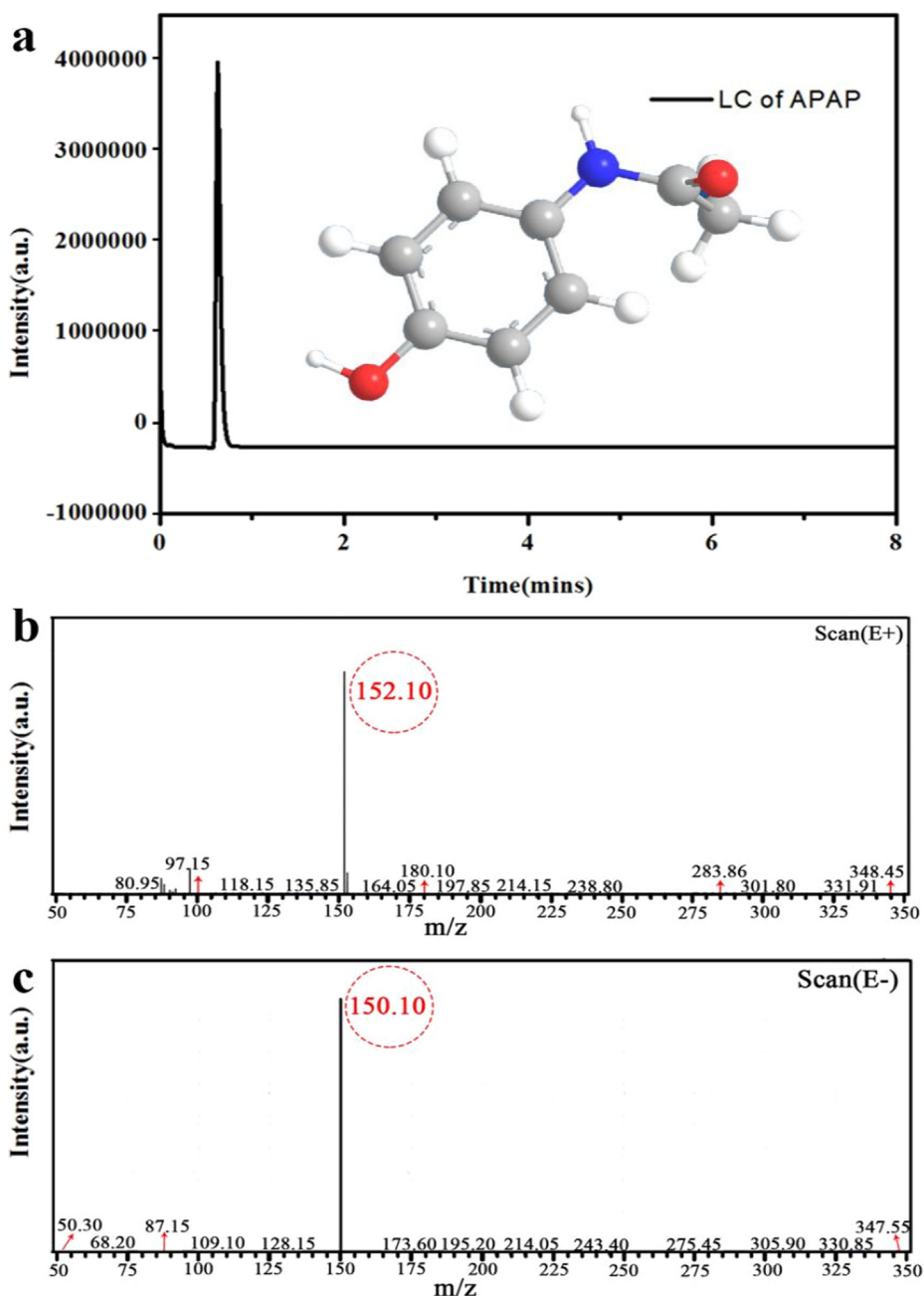


Fig. 6 LC-MS results of APAP (a), (b) and (c).

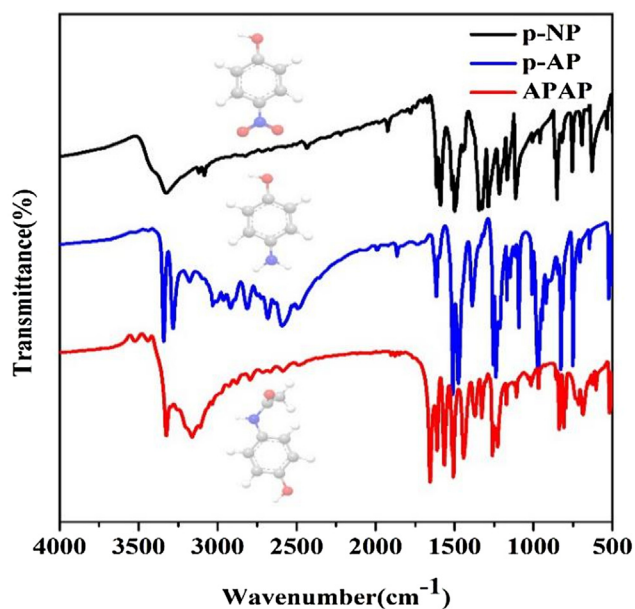


Fig. 7 The IR results of the initial p-NP, the reduced intermediate p-AP and the final product APAP.

and 152.10 (Fig. 6b and c), respectively (Golizeh et al., 2015). Eventually, an excellent conversion about 85% productivity of APAP from p-NP is achieved.

The FT-IR spectrum was also tested for the intermediate and product (Fig. 7). Two peaks in the range of 3400.00–3200.00 cm^{-1} correspond to $-\text{NH}_2$ stretching vibrations of ns (NH_2), as well as the $\text{d}(\text{NH}_2)$ at 1650.00 cm^{-1} for p-AP (Reddy et al., 2018; Shimizu et al., 2010). No peaks corresponded to $-\text{NO}_2$ in the spectra indicates the utterly reduction of p-NP. The IR peak of APAP displayed at 3161.00 cm^{-1} (one O-H stretching) is originated from the hydrogen bonding of phenol, and other characteristic IR peaks are C=C ring stretch bands (1650.00, 1563.00, 1507.00 and 1438.00 cm^{-1}), overtone combination bands (1851.33 cm^{-1} and 2115.53 cm^{-1}) and out of plane C-H bending (802.24 cm^{-1}), respectively (Gao et al., 2017). In addition, the peak of the nas (NH_2) at 3447.00 cm^{-1} is markedly shifted negative (Ding et al., 2010). The amide functional group is evidenced by a sharp N-H stretch at 3323.00 cm^{-1} ; a strong C=O stretch of amide I band at 1653.66 cm^{-1} , and an amide II band at 1563.00 cm^{-1} due to a combination of N-H bending and C-N stretching (Ding et al., 2010). Thus all of the peaks in IR ensure the generation of APAP. These results show that in view points of availability, efficiency, and reusability of the catalyst, the present protocol is comparable efficient.

3.3. Investigation on the mechanism of p-NP conversion and APAP synthesis

Obviously, the quickly selective conversion of p-NP to p-AP is vital rate-determining step in our designed synthesized route of APAP for the required productivity and purity. As identification above (Figs. 5 and 6), $\text{Cu}_2\text{O}@/\text{CeO}_2$ nanocomposites give a very excellent selective conversion for p-NP to sole product of p-AP. To understand such mechanism, the structural evolution for initial and final catalyst was recognized by the wide-

scan XPS spectra (Fig. 8). It is noted that although the elemental species are not at all various during the reactive proceeding (Fig. 8a and b), the valence states of Cu and Ce species are substantially diverse. The peak of Cu element is fitted into three peaks of Cu^+ 2p_{3/2} with the binding energies at 932.5, 933.2 and 934.5 eV, for the initial samples (Fig. 8c). Furthermore, the small peaks at binding energies 933.8 eV, 953.7 eV in Cu 2p spectra, together with two shakeup peaks, are all assigned to Cu^{2+} , confirming the presence of small amount of CuO on the surface of the catalyst (Espinosa et al., 2002). However, after the reaction, CuO disappears while pure Cu^0 appears at 952.5 eV (Fig. 8d). Obviously, the electron-enriched Cu^0 is formed via gradually reducing $\text{Cu}^{2+} \rightarrow \text{Cu}^+ \rightarrow \text{Cu}^0$ during the reaction proceeding, which may easily extract hydrogen from NaBH_4 to form Cu-H species and then to promote the reduced reaction. Actually, several researches have reported Cu^+ , Cu^{2+} , and Cu^0 are all active substances in the borohydride mediated reduction of nitroarenes (Wang et al., 2016; Zhang et al., 2017). Furthermore, by inspecting the characteristic peak positions associated with cerium element (Fig. 8e and f, Table S2), four peaks at 916.3, 907.3, 902.2, and 900.4 eV observed in Ce 3d_{3/2} profile are corresponding to the α_1 , α_2 , α_3 , and α_4 components. Meanwhile the peaks of Ce 3d_{5/2} profile at 898.0, 888.5, 883.5, and 881.9 eV are assigned to the β_1 , β_2 , β_3 , and β_4 constituents, respectively (Gao et al., 2017; Wang et al., 2014). As it known, the signals α_3 and β_3 are characteristics of Ce^{3+} , quite distinctly demonstrating the existence of Ce^{3+} in $3\text{Cu}_2\text{O}@/\text{CeO}_2$.

Fig. 9 shows the X-band EPR signal of CeO_2 and $3\text{Cu}_2\text{O}@/\text{CeO}_2$ which could also provide a direct evidence for the existence of Ce^{3+} . Two signals at 3125.0 G and 3125.3 G were observed for CeO_2 . Two peaks show the g-value spectra of the CeO_2 nanostructure, which indicates the presence of a narrow signal at $g = 1.96$ and a strong signal at $g \approx 2.00$. It has reported CeO_2 will release lattice oxygen to form the oxygen vacancies in the case of Ce^{4+} becoming Ce^{3+} (Damyanova et al., 2018). In the present investigation, there obviously are higher concentrations of Ce^{3+} ions and corresponding oxygen vacancies in the prepared composite samples. As it is known, the rate determining step of the present reaction is the reduction of adsorbed p-nitrophenolate by active hydrogen species (Ji et al., 2014). Thus a rapid and directed pre-adsorption of p-NP on the surface of catalyst play a vital role to accelerate reaction process and achieve high selectivity. In view of this, the presence of Ce^{3+} ions and oxygen vacancies in the prepared sample have significant advantages in the oriented adsorption and selective reduction. The adsorption of p-NP was tested with the same condition of p-NP reduction only without NaBH_4 . Obviously, the smooth cuprous oxide can never absorbed p-NP which is assigned to the large particles with the flat surfaces (Fig. 10a). The oxygen-deficient CeO_2 surface preferentially provides the promising active site for the adsorption of nitroarene by capturing the oxygen atom of $-\text{NO}_2$ (Fig. 10b). The high selectivity is finally dedicated by $\text{Cu}_2\text{O}/\text{CeO}_2$ interface of catalyst that could regulate the adsorption to preferentially activate $-\text{NO}_2$ group (Fig. 10c). Furthermore, when nitro groups are reduced to amino, it will be released from the catalytic surface as a neutral compound (Fig. 10d). The IR spectrum of the as-prepared $3\text{Cu}_2\text{O}@/\text{CeO}_2$ before and after adsorption of p-NP listed in Fig. S5 also indicates that core-shell nanocomposite could effectively absorb p-NP. In addition, as it tested, CeO_2 in aqueous medium

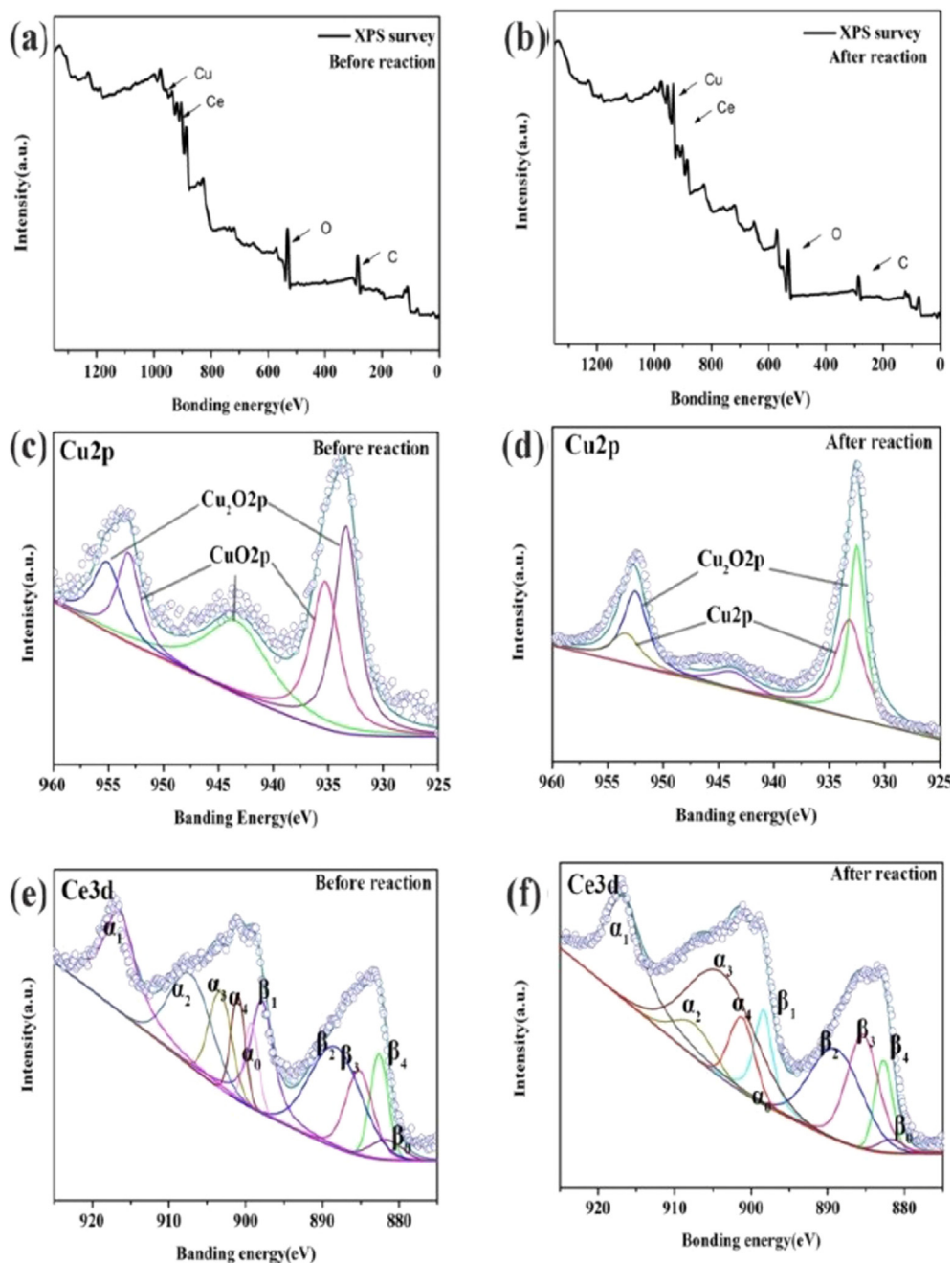


Fig. 8 The XPS spectrum (a, b), single element scan spectra of Ce3d (c, d), and Cu2p (e, f) of the initial and the used 3Cu₂O@CeO₂.

(PH = 7) exhibits negative zeta potential values (Fig. S6). Thus, the constituents Cu₂O and Cu (in situ generated) may contribute to adsorb BH₄⁻ anions but CeO₂ does not in terms of the electrostatic repulsion.

Furthermore, the electrochemical impedance spectroscopy (EIS) and photoluminescence spectra (PL) of CeO₂, Cu₂O and 3Cu₂O@CeO₂ (Fig. 11) were used to measure electron transmission due to their important role in the quick reduction proceeding. The curve radius of 3Cu₂O@CeO₂ is much lower than that of cuprous oxide, indicating that the electron transport capability is greatly improved (Fig. 11a). In addition, the PL emission intensity and peak width of CeO₂ is stronger than

both Cu₂O and Cu₂O@CeO₂ (Fig. 11b). It means larger amount of valence electrons can be excited to the defect states (oxygen vacancies) and thus the larger emission signal will be received (Zhang et al., 2014). Remarkably, component CeO₂ responses electronic transport and Cu₂O contributes to inhibit electronic recombination with the remained hole. On the other hand, the electrons tend to leave CeO₂ to Cu₂O and Cu⁰ when assembly them to form the composite in considering of the fact that the Fermi energy level of CeO₂ (0–1.9 eV) is lower than that of Cu₂O (2.7 eV) and even Cu⁰ (2.0 eV). Due to the electron transfer, an electron-enriched Cu⁰ is produced which beneficial to the extract H species form BH₄ to form M-H. It

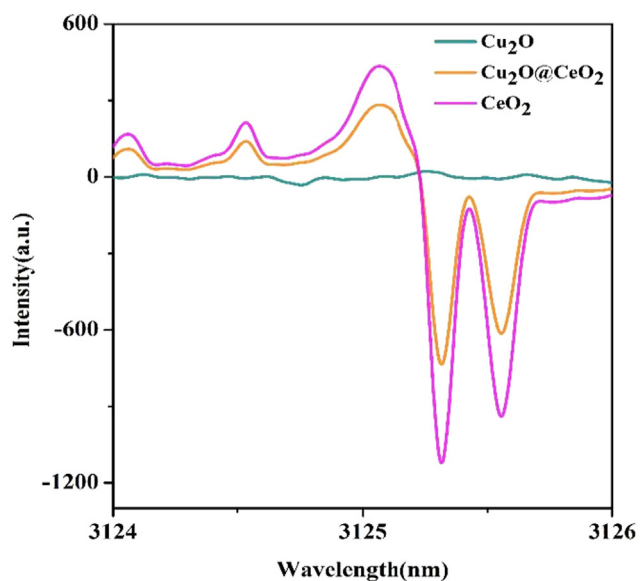


Fig. 9 EPR spectra of CeO_2 and $3\text{Cu}_2\text{O}@/\text{CeO}_2$.

indicates that the valence variation $\text{Cu}^+ \rightarrow \text{Cu}^0$ coupled with $\text{Ce}^{3+} \rightarrow \text{Ce}^{4+}$ is expected to be beneficial for the sustained selective reduction of p-NP.

In summary, a possible mechanism for the selective conversion of p-NP to p-AP with $\text{Cu}_2\text{O}@/\text{CeO}_2$ was obtained (Fig. 12). It is postulated that highly electron-enriched Cu^0 was generated in situ from Cu_2O through $\text{Ce}^{4+} - \text{Ce}^{3+} \rightarrow \text{Cu}^+ - \text{Cu}^0$ coupled redox. The generated Cu^0 extracts hydrogen species from hydrogen-donor and then transfers H species to converse p-NP into p-AP. Oxygen deficiency on the surface of cerium oxide captures directionally the oxygen atom of $-\text{NO}_2$ from p-NP and preferentially provides an electron transfer site from BH_4^- to a recipient p-NP, resulting in the selective conversion of the nitroaromatic compounds. At the same time, the close contact between CeO_2 shell and Cu_2O core also play a key role in quickly electron transformation from BH_4^- to p-nitrophenolate ions. Meanwhile, $\text{Cu}^{2+}/\text{Cu}^+$ and $\text{Ce}^{4+}/\text{Ce}^{3+}$ redox was maintained through the interaction of Cu and Ce to continuously furnish p-AP. The neutrally charged intermediate product (p-AP) is released from cerium oxide hence the active sites of the surface of the materials are again exposed,

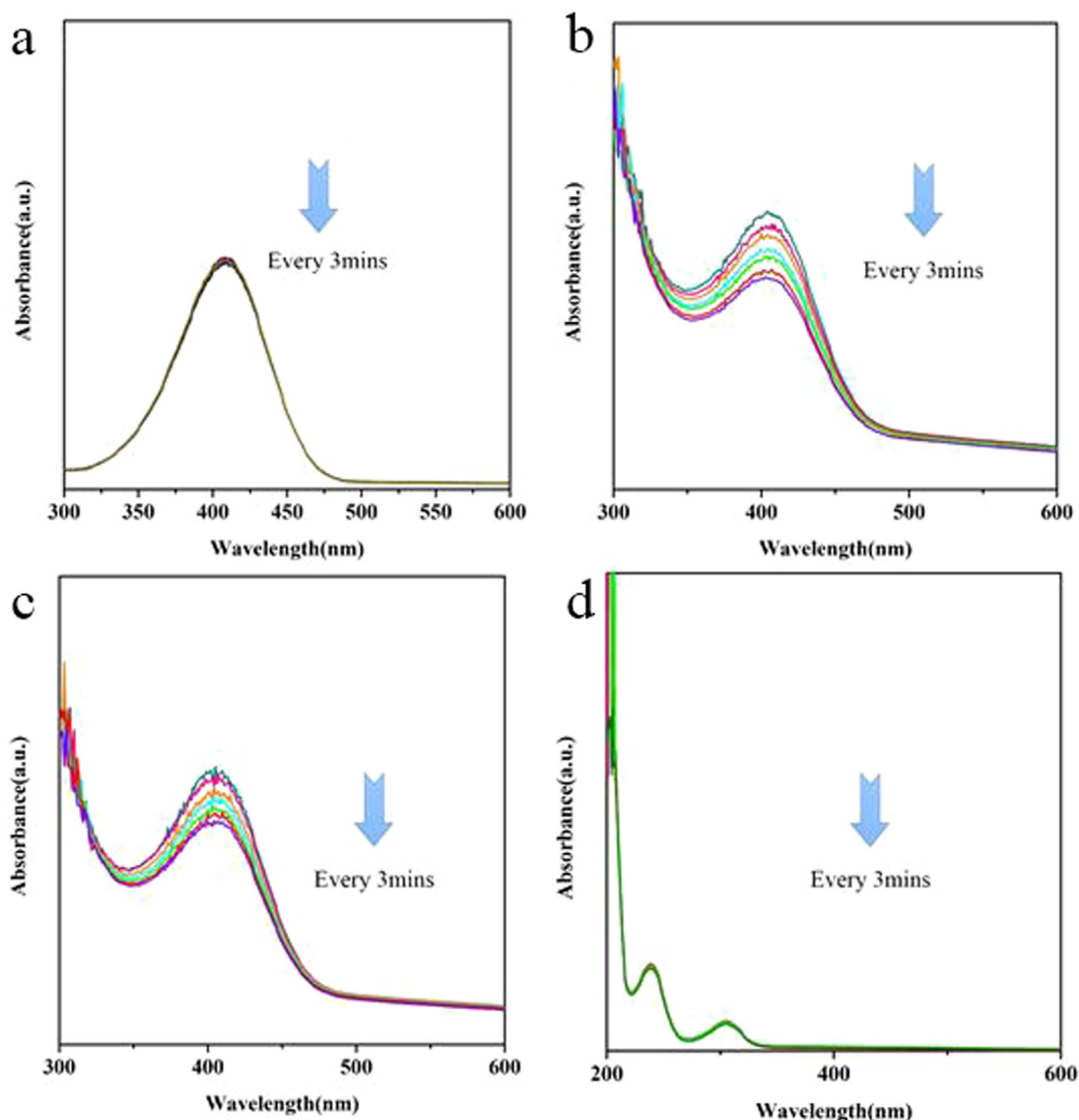


Fig. 10 The absorption of (a) p-AP with Cu_2O , (b) p-NP with CeO_2 , (c) p-NP with $3\text{CeO}_2@/\text{Cu}_2\text{O}$, and (d) p-AP with $3\text{CeO}_2@/\text{Cu}_2\text{O}$.

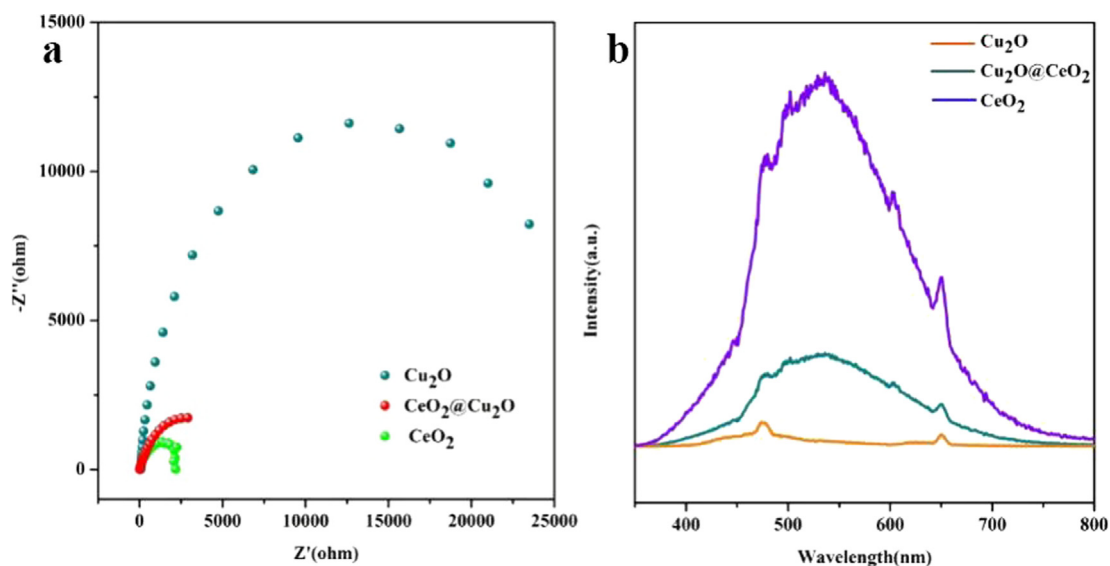


Fig. 11 (a) the EIS spectrum and (b) the PL spectrum of 3Cu₂O@CeO₂, CeO₂ and Cu₂O.

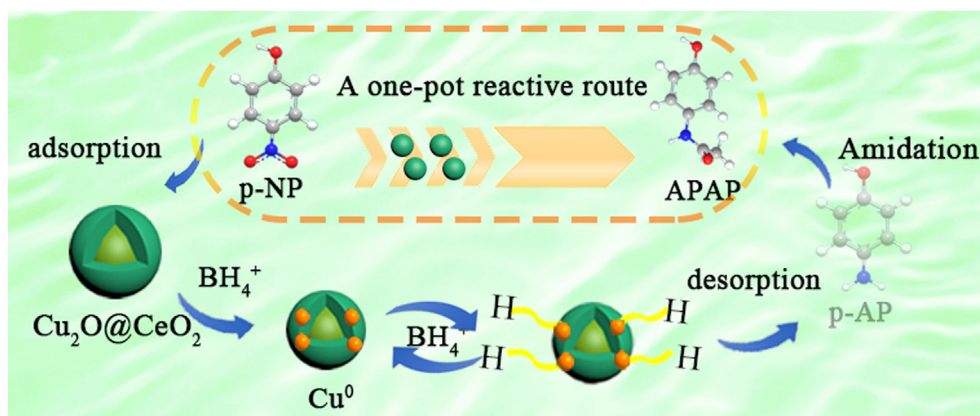


Fig. 12 Mechanism of conversion p-NP to P-AP and then APAP.

leading to the next cycle reaction of precursors (p-NP and BH₄⁺) smoothly proceeds. The highly selective generation of p-AP effectively inhibits the by-products. The subsequently quick acylation of intermediate p-AP and quick separation of final products by negative pressure methods maximize the yield and purity of APAP. Eventually, APAP was prepared by catalytic hydrogenation and acetylation using p-NP as a starting material.

4. Conclusion

In this study, a simple and efficient protocol has been developed to synthesize APAP by using p-NP as the initial reactant with a core-shell Cu₂O@CeO₂ as catalyst. A one-pot reactive route with two sections included the selectively hydrogenation of p-NP and alkylation of generated p-AP was meticulously designed and went smoothly with a self-constructing device. The key intermediate p-AP could be continually formed by the prepared Cu₂O@CeO₂ which has been confirmed with an extended sustainable usability during 30 experimental turns. The excellent productivity (about 85%) of APAP with a high

purity are obtained by the quick acylation of the intermediate p-AP to effectively avoid the coupling byproducts occurrence with the designed reactive device. The structure of the intermediates and final products were characterized by IR, HNMR, and LC-MS. The proposed mechanism is that CeO₂ shell coated on Cu₂O is used as a stabilizer and adsorptive centers, owing to the existence of Ce³⁺ ions and oxygen vacancies. The valence variation Cu⁺ → Cu⁰ coupled with Ce³⁺ → Ce⁴⁺ is expected to be beneficial for the sustained selective conversion of p-NP to p-AP, a rate-determining step in the present synthesized reaction. Compared to the traditional methods by using nitroaromatic compounds as the raw materials, the current proposed synthesis route of APAP presents the merits with low-cost, easy-operation, high-efficiency and high purity.

Acknowledgements

The authors would like to thank these financial supports from National Natural Science Foundation of China (Grants 21777078 and 22062016), the Major Project of Inner Mongolia Natural Science Foundation (Grants 2020ZD02), and the Pro-

ject of Research and Development of the Applied Technology for Inner Mongolia of China (Grants 2020SGG0065).

Appendix A. Supplementary data

Supplementary data to this article can be found online at <https://doi.org/10.1016/j.arabjc.2020.09.047>.

References

- Arulraj, A.D., Vijayan, M., Vasantha, V.S., 2015. Highly selective and sensitive simple sensor based on electrochemically treated nanopolyrrole-sodium dodecyl sulphate film for the detection of par-nitrophenol. *Anal Chim Acta.* 899, 66–74.
- Bai, S., Shen, X., Zhu, G., Li, M., Xi, H., Chen, K., 2012. In situ growth of Ni(x)Co(100-x) nanoparticles on reduced graphene oxide nanosheets and their magnetic and catalytic properties. *ACS Appl Mater Interfaces.* 4, 2378–2386.
- Blaser, H.U., Steiner, H., Studer, M., 2009. Selective catalytic hydrogenation of functionalized nitroarenes: An update. *Chem-CatChem* 1, 210–221.
- Chen, H., Yang, M., Tao, S., Chen, G., 2017. Oxygen vacancy enhanced catalytic activity of reduced Co₃O₄ towards p-nitrophenol reduction. *Appl. Catal. B* 209, 648–656.
- Christians, J.A., Fung, R.C., Kamat, P.V., 2014. An inorganic hole conductor for organo-lead halide perovskite solar cells Improved hole conductivity with copper iodide. *J. Am. Chem. Soc.* 136, 758–764.
- Corma, A., Serna, P., 2006. Chemoselective hydrogenation of nitro compounds with supported gold catalysts. *Science* 313, 332–334.
- Damyanova, S., Pawelec, B., Palcheva, R., Karakirova, Y., Sanchez, M.C.C., Tyuliev, G., Gaigneaux, E., Fierro, J.L.G., 2018. Structure and surface properties of ceria-modified Ni-based catalysts for hydrogen production. *Appl. Catal. B* 225, 340–353.
- Das, R., Sypu, V.S., Paumo, H.K., Bhaumik, M., Maharaj, V., Maity, A., 2019. Silver decorated magnetic nanocomposite (Fe₃O₄@PPy-MAA/Ag) as highly active catalyst towards reduction of 4-nitrophenol and toxic organic dyes. *Appl. Catal. B* 244, 546–558.
- Ding, L., He, J., Huang, L., Lu, R., 2010. Studies on a novel modified β -cyclodextrin inclusion complex. *J. Mol. Struct.* 979, 122–127.
- Espinosa, J.P., Morales, J., Barranco, A., Caballero, A., Holgado, J.P., Gonzalez-Eliphe, A.R., 2002. Interface effects for Cu, CuO, and Cu₂O deposited on SiO₂ and ZrO₂. XPS determination of the valence state of Copper in Cu/SiO₂ and Cu/ZrO₂ Catalysts. *J. Phys. Chem. B.* 106, 6921–6929.
- Evangelista, V., Acosta, B., Miridonov, S., Smolentseva, E., Fuentes, S., Simakov, A., 2015. Highly active Au-CeO₂@ZrO₂ yolk-shell nanoreactors for the reduction of 4-nitrophenol to 4-aminophenol. *Appl. Catal. B* 166, 518–528.
- Formenti, D., Ferretti, F., Scharnagl, F.K., Beller, M., 2019. Reduction of nitro compounds using 3d-non-noble metal catalysts. *Chem Rev.* 119, 2611–2680.
- S. Fountoulaki, V. Daikopoulou, P. L. Gkizis, I. Tamiolakis, G. S. Armatas, and I.N. Lykakis Mechanistic studies of the reduction of nitroarenes by NaBH₄ or hydrosilanes catalyzed by supported gold nanoparticles, *ACS Catal.* 4(2014) 3504–3511.
- Gao, F., Tang, X., Yi, H., Li, J., Zhao, S., Wang, J., Chu, C., Li, C., 2017. Promotional mechanisms of activity and SO₂ tolerance of Co- or Ni-doped MnOx-CeO₂ catalysts for SCR of NOx with NH₃ at low temperature. *Chem. Eng. J.* 317, 20–31.
- Golizeh, M., LeBlanc, A., Sleno, L., 2015. Identification of acetaminophen adducts of rat liver microsomal proteins using 2D-LC-MS/MS. *Chem. Res. Toxicol.* 28, 2142–2150.
- Han, A., Zhang, J., Sun, W., Chen, W., Zhang, S., Han, Y., Feng, Q., Zheng, L., Gu, L., Chen, C., Peng, Q., Wang, D., Li, Y., 2019. Isolating contiguous Pt atoms and forming Pt-Zn intermetallic nanoparticles to regulate selectivity in 4-nitrophenylacetylene hydrogenation. *Nat. Commun.* 10, 3787.
- Haniti, M., Hamid, S.A., Allen, C.L., Gareth, W., 2009. Ruthenium-catalyzed N-alkylation of amines and sulfonamides using borrowing hydrogen methodology. *J. Am. Chem. Soc.* 131, 1766–1774.
- Huang, C., Ye, W., Liu, Q., Qiu, X., 2014. Dispersed Cu(2)O octahedrons on h-BN nanosheets for p-nitrophenol reduction. *ACS Appl. Mater Interfaces.* 6, 14469–14476.
- Ji, Z., Shen, X., Yang, J., Zhu, G., Chen, K., 2014. A novel reduced graphene oxide/Ag/CeO₂ ternary nanocomposite: Green synthesis and catalytic properties. *Appl. Catal. B* 144, 454–461.
- Li, J., Song, S., Long, Y., Wu, L., Wang, X., Xing, Y., Jin, R., Liu, X., Zhang, H., 2018. Investigating the hybrid-structure-effect of CeO₂-encapsulated Au nanostructures on the transfer coupling of nitrobenzene. *Adv Mater.* 30.
- Li, H., Xu, C., Mu, X.-L., Zhang, P., Zhang, X.-M., Zheng, N., 2018. Acetylene mediated synthesis of supported Pt nanocatalyst for selective hydrogenation of halonitrobenzene. *Chem. Nano Mat.* 4, 518–523.
- Liu, Y., Jiang, G., Li, L., Chen, H., Huang, Q., Jiang, T., Du, X., Chen, W., 2015. Preparation of Au/PAN nanofibrous membranes for catalytic reduction of 4-nitrophenol. *J. Mater. Sci.* 50, 8120–8127.
- Liu, Y., Wang, Q., Wu, L., Long, Y., Li, J., Song, S., Zhang, H., 2019. Tunable bimetallic Au-Pd@CeO₂ for semihydrogenation of phenylacetylene by ammonia borane. *Nanoscale.* 11, 12932–12937.
- Lum, Y., Ager, J.W., 2018. Stability of residual oxides in oxide-derived copper catalysts for electrochemical CO₂ reduction investigated with (18) O labeling. *Angew. Chem. Int. Ed. Engl.* 57, 551–554.
- Macino, M., Barnes, A.J., Althahban, S.M., Qu, R., Gibson, E.K., Morgan, D.J., Freakley, S.J., Dimitratos, N., Kiely, C.J., Gao, X., Beale, A.M., Bethell, D., He, Q., Sankar, M., Hutchings, G.J., 2019. Tuning of catalytic sites in Pt/TiO₂ catalysts for the chemoselective hydrogenation of 3-nitrostyrene. *Nat. Catal.* 2, 873–881.
- Magadam, D.B., Yadav, G.D., 2018. Chemoselective Acetylation of 2-aminophenol using immobilized lipase: process optimization, mechanism, and kinetics. *ACS Omega* 3, 18528–18534.
- Ozel, F., Sarilmaz, A., Istanbulu, B., Aljabour, A., Kus, M., Sonmezoglu, S., 2016. Penternary chalcogenides nanocrystals as catalytic materials for efficient counter electrodes in dye-sensitized solar cells. *Sci. Rep.* 6, 29207.
- Qi, J., Chen, J., Li, G., Li, S., Gao, Y., Tang, Z., 2012. Facile synthesis of core-shell Au@CeO₂ nanocomposites with remarkably enhanced catalytic activity for CO oxidation. *Energy Environ. Sci.* 5, 8937.
- Qiu, X., Liu, Q., Song, M., Huang, C., 2016. Hydrogenation of nitroarenes into aromatic amines over Ag@BCN colloidal catalysts. *J. Colloid Interface Sci.* 477, 131–137.
- Reddy, Y.V.M., Bathinapatla, S., Łuczak, T., Osińska, M., Maseed, H., Ragavendra, P., Sarma, L.S., Srikanth, V.V.S.S., Madhavi, G., 2018. An ultra-sensitive electrochemical sensor for the detection of acetaminophen in the presence of etilefrine using bimetallic Pd-Ag/reduced graphene oxide nanocomposites. *New J. Chem.* 42, 3137–3146.
- Ren, Z.H., Li, H.T., Gao, Q., Wang, H., Han, B., Xia, K.S., Zhou, C. G., 2017. Au nanoparticles embedded on urchin-like TiO₂ nanosphere: an efficient catalyst for dyes degradation and 4-nitrophenol reduction. *Mater. Des.* 121, 167–175.
- Z. Rong, W. Zhang, P. Zhang, Z. Sun, J. Iv, W. Du, Y. Wang, One-pot synthesis of N,N-dimethylanilines from nitroarenes with skeletal Cu as chemoselective catalyst, *Catalysis Communications.* 41 (2013) 115-118.
- Serna, P., Corma, A., 2015. Transforming nano metal nonselective particulates into chemoselective catalysts for hydrogenation of substituted nitrobenzenes. *ACS Catal.* 5, 7114–7121.
- Shimizu, K.I., Miyamoto, Y., Satsuma, A., 2010. Size- and support-dependent silver cluster catalysis for chemoselective hydrogenation of nitroaromatics. *J. Catal.* 270, 86–94.

- Shokouhimehr, M., Hong, K., Lee, T.H., Moon, C.W., Hong, S.P., Zhang, K., Suh, J.M., Choi, K.S., Varma, R.S., Jang, H.W., 2018. Magnetically retrievable nanocomposite adorned with Pd nanocatalysts: efficient reduction of nitroaromatics in aqueous media. *Green Chem.* 20, 3809–3817.
- Song, J., Huang, Z.-F., Pan, L., Li, K., Zhang, X., Wang, L., Zou, J.-J., 2018. Review on selective hydrogenation of nitroarene by catalytic, photocatalytic and electrocatalytic reactions. *Appl. Catal. B* 227, 386–408.
- Song, S., Liu, X., Li, J., Pan, J., Wang, F., Xing, Y., Wang, X., Liu, X., Zhang, H., 2017. Confining the nucleation of Pt to in situ form (Pt-Enriched Cage)@CeO₂ Core@Shell nanostructure as excellent catalysts for hydrogenation reactions. *Adv Mater.* 29.
- Sun, J., Fu, Y., He, G., Sun, X., Wang, X., 2014. Catalytic hydrogenation of nitrophenols and nitrotoluenes over a palladium/graphene nanocomposite. *Catal. Sci. Technol.* 4, 1742–1748.
- Takasaki, M., Motoyama, Y., Higashi, K., Yoon, S.-H., Mochida, I., Nagashima, H., 2008. Chemoselective hydrogenation of nitroarenes with carbon nanofiber-supported platinum and palladium nanoparticles. *Org. Lett.* 10, 1601.
- Toe, C.Y., Zheng, Z., Wu, H., Scott, J., Amal, R., Ng, Y.H., 2018. Photocorrosion of cuprous oxide in hydrogen production: Rationalising self-oxidation or self-reduction. *Angew. Chem. Int. Ed Engl.* 57, 13613–13617.
- Tsujii, T., Zaoputra, A.A., Hitomi, Y., Mieda, K., Ogura, T., Shiota, Y., Yoshizawa, K., Sato, H., Kodera, M., 2017. Specific enhancement of catalytic activity by a dicopper core: selective hydroxylation of benzene to phenol with hydrogen peroxide. *Angew Chem Int Ed Engl.* 56, 7779–7782.
- Wang, D., Astruc, D., 2017. The recent development of efficient Earth-abundant transition-metal nanocatalysts. *Chem. Soc. Rev.* 46, 816–854.
- Wang, F., Büchel, R., Savitsky, A., Zalibera, M., Widmann, D., Pratsinis, S.E., Lubitz, W., Schüth, F., 2016. In situ EPR study of the redox properties of CuO–CeO₂ Catalysts for preferential CO oxidation (PROX). *ACS Catal.* 6, 3520–3530.
- Wang, Z.H., Fu, H.F., Han, D.M., Gu, F.B., 2014. The effects of Au species and surfactant on the catalytic reduction of 4-nitrophenol by Au@SiO₂. *J. Mater. Chem. A* 2, 20374–20381.
- Wang, F., Li, W., Feng, X., Liu, D., Zhang, Y., 2016. Decoration of Pt on Cu/Co double-doped CeO₂ nanospheres and their greatly enhanced catalytic activity. *Chem Sci.* 7, 1867–1873.
- Wang, Y., Wang, F., Chen, Y., Zhang, D., Li, B., Kang, S., Li, X., Cui, L., 2014. Enhanced photocatalytic performance of ordered mesoporous Fe-doped CeO₂ catalysts for the reduction of CO₂ with H₂O under simulated solar irradiation. *Appl. Catal. B* 147, 602–609.
- Wu, Y., Li, C., Zhou, K., Zhao, Y., Wang, X., 2016. A new preparation strategy via an in situ catalytic process: CeO₂@Ag/Ag₂Ta₄O₁₁ catalyst for 4-nitrophenol reduction. *CrystEngComm* 18, 6513–6519.
- Xu, L., Li, X., Zhu, Y., Xiang, Y., 2009. One-pot synthesis of N, N-dimethylaniline from nitrobenzene and methanol. *New J. Chem.* 33, 2051.
- Xuan, S., Wang, Y.X., Yu, J.C., Leung, K.C., 2009. Preparation, characterization, and catalytic activity of core/shell Fe₃O₄@-polyaniline@Au nanocomposites. *Langmuir* 25, 11835–11843.
- Yu, T., Zeng, J., Lim, B., Xia, Y., 2010. Aqueous-phase synthesis of Pt/CeO₂ hybrid nanostructures and their catalytic properties. *Adv Mater.* 22, 5188–5192.
- Zhang, X., Qin, J., Xue, Y., Yu, P., Zhang, B., Wang, L., Liu, R., 2014. Effect of aspect ratio and surface defects on the photocatalytic activity of ZnO nanorods. *Sci Rep.* 4, 4596.
- Zhang, J., Zhou, T., Wen, L., 2017. Selective metallization induced by laser activation: fabricating metallized patterns on polymer via metal oxide composite. *ACS Appl Mater Interfaces.* 9, 8996–9005.
- Zhang, Y., Zhu, P., Li, G., Cui, Z., Cui, C., Zhang, K., Gao, J., Chen, X., Zhang, G., Sun, R., Wong, C., 2019. PVP-mediated galvanic replacement synthesis of smart elliptic Cu-Ag Nanoflakes for electrically conductive pastes. *ACS Appl Mater Interfaces* 11, 8382–8390.
- Zhao, Y., Li, R., Jiang, P., Zhang, K., Dong, Y., Xie, W., 2019. Mechanistic study of catalytic hydride reduction of –NO₂ to –NH₂ using isotopic solvent and reducer: the real hydrogen source. *J. Phys. Chem. C.* 123, 15582–15588.
- Zhuang, Y.T., Gao, W., Yu, Y.L., Wang, J.H., 2017. Facile fabrication of three-dimensional porous CuFe₂O₄ cages as highly efficient and recyclable heterogeneous catalyst. *Mater. Des.* 130, 294–301.